Achieving Near-Atomic Resolution in Single-Particle Cryo-EM Using a Single Micrograph

Zi Yang[1,2,3,4#], Xiao Fan[1,2,3,5#], Hong-Wei Wang[1,2,3*]

[1] Ministry of Education Key Laboratory of Protein Sciences, Beijing Frontier Research Center of Biological Structures, School of Life Sciences, Tsinghua University, Beijing, China

[2] Tsinghua-Peking Joint Center for Life Sciences, Tsinghua University, Beijing, China

[3] Beijing Advanced Innovation Center for Structural Biology, Tsinghua University, Beijing, China

[4] Present address: Department of Molecular Biophysics and Biochemistry, Yale University, New Haven, CT 06511, USA

[5] Present address: Institute of Bio-Architecture and Bio-Interactions (IBABI), Shenzhen Medical Academy of Research and Translation (SMART), Shenzhen 518107, Guangdong, China.

[#] These authors contributed equally: Zi Yang, Xiao Fan

* Correspondence should be addressed to H.-W.W. (E-mail: hongweiwang@tsinghua.edu.cn)

Declaration

The Chinese version of this work was published in the *Journal of Chinese Electron Microscopy Society*. To facilitate sharing with international readers, the content has been reorganized and prepared as an English-language manuscript. This English manuscript has not been published previously in any journal or posted on any preprint platform, and its English release has been approved by the *Journal of Chinese Electron Microscopy Society*.

Original Chinese version:
http://www.dzxwxb.ac.cn/index.php?m=content&c=index&a=show&catid=146&id=1332

Abstract

Single-particle cryo-electron microscopy (cryo-EM) typically requires the acquisition and analysis of a large number of micrographs to achieve high-resolution three-dimensional (3D) reconstructions of biological macromolecules. In this study, we demonstrate that when sample quality is sufficiently high, near-atomic resolution 3D density maps can be obtained using particle images from a single cryo-EM micrograph. Using this approach, we successfully reconstructed the 3D structures of apoferritin and the 20S proteasome from single-micrograph datasets. Our analysis reveals that the zero-crossings in the single-micrograph contrast transfer function (CTF) can be compensated by variations in the axial (Z-axis) distribution of particles within the vitrified sample and the intrinsic astigmatism of the optical system, thereby effectively recovering structural information across the full range of spatial frequencies. Furthermore, by analyzing reconstructions from dose-fractionated frames with varying cumulative electron exposures, we found that the minimal electron dose required to preserve undamaged high-frequency information while maintain sufficient low-frequency signals for accurate orientation determination is substantially lower than the commonly applied total doses. Based on this, we estimate the theoretical lower bounds of both electron dose and particle number required for high-resolution structure determination. This work advances our understanding of signal preservation in cryo-EM imaging and provides practical insight for optimizing data acquisition strategies to maximize retention of high-frequency structural information.

Introduction

In recent years, single-particle cryo-electron microscopy (cryo-EM) has been propelled to the forefront of structural biology. This technique enables the visualization of biological macromolecules at near-atomic resolution in states close to their native environments[1]. Unlike X-ray crystallography, cryo-EM single-particle analysis (SPA) does not require crystallization of target proteins. Instead, it achieves high-resolution reconstructions directly from two-dimensional projections of individual particles, making it particularly well-suited for studying large macromolecular complexes and membrane proteins that are difficult or impossible to crystallize[2]. Since 2013, cryo-EM has entered the so-called "resolution revolution"[3] and has undergone rapid advancements over the past decade. As an ever-increasing number of near-atomic resolution bio-macromolecular structures have been determined, cryo-EM has established itself as a mainstream method for high-resolution structural determination[4-7].

These achievements have been driven by advances such as the direct electron detectors with enhanced detective quantum efficiency (DQE)[8], dose-fractionated movie acquisition strategies[9], and the implementation of Bayesian-based image processing algorithms[10]. Together, these innovations have significantly improved the recovery of high-frequency structural details from inherently noisy cryo-EM images[11], pushing the detectable limits of molecular size and attainable resolution. In parallel, automated data collection workflows and optimized imaging strategies have greatly increased the throughput and efficiency of data acquisition in SPA.

Despite these advances, the radiation sensitivity of biological specimens and the inherently low signal-to-noise ratio (SNR) of low-dose cryo-EM images[12] necessitate the use of large particle datasets in common SPA workflows, thereby achieving enhanced SNR via averaging and complete Fourier space interpolation through dense angular sampling[2]. Analysis of Electron Microscopy Data Bank (EMDB) entries indicates that most current high-resolution reconstructions rely on tens of thousands to millions of particle images extracted from large numbers of micrographs, imposing substantial demands on data collection and computation. The theoretical models proposed by Henderson *et al.* allow the estimation of the minimum particle number required to achieve a target resolution for a given macromolecule[13]. Notably, under optimal sample and imaging conditions, high-resolution structures of apoferritin have been reconstructed using fewer than 1,000 particles[14]. Nevertheless, particles must still be selected

from micrographs with varying defocus values to compensate for zero-crossings, which degrade image information at specific spatial frequencies, in the oscillatory contrast transfer function (CTF). To further accelerate cryo-EM SPA, it is essential not only to improve the efficiency of data acquisition and processing, but also to explore the theoretical limits of the minimum number of particle images or lowest electron dose required for near-atomic resolution reconstruction.

In bright-field transmission electron microscopy (TEM), detected images are modulated and distorted by the CTF, which arises primarily from the defocus and spherical aberration. In Fourier space, the CTF oscillates with spatial frequency, alternating in sign and producing zero crossings at which signal is completely lost. For a given microscope, the positions of CTF zeroes depend directly on the defocus used during image formation.

The CTF can be mathematically described as:

$$H(k) = \sin[(2\pi)\gamma(k)] \tag{1}$$

$$\gamma(k) = -\frac{1}{2}z\lambda k^2 + \frac{1}{4}C_s\lambda^3 k^4 \tag{2}$$

where *H(k)* is the CTF, λ represents the electron wavelength, *k* is the spatial frequency, *z* is the defocus, and *Cs* is the spherical aberration coefficient of the objective lens. Phase shift *γ(k)* is induced by defocus z and spherical aberration *Cs* as shown in Equation (1).

To capture complete structural information across the full range of spatial frequencies, micrographs are typically acquired at a series of defocus values to compensate for signal loss caused by the CTF. This approach provides complementary coverage of spatial frequencies that would otherwise be attenuated or lost due to CTF zero-crossings. However, when working with small datasets with reduced the number of micrographs or particle images for three-dimensional reconstruction, it becomes critical to carefully evaluate how CTF-induced signal attenuation is compensated. Investigating mechanisms to recover information lost near the CTF zero-crossings will help elucidate how imaging conditions and data acquisition strategies influence the quality and resolution of cryo-EM reconstructions.

In this study, we demonstrate that near-atomic resolution 3D reconstructions can be achieved from single cryo-EM micrographs using relatively small numbers of particles. Specifically, we obtained a 2.9 Å reconstruction of apoferritin using approximately 300 particles and a 3.4 Å reconstruction of the 20S proteasome from approximately 400 particles, each derived from a single micrograph. Comparable results were also obtained from publicly available apoferritin datasets. These reconstructions exhibit continuous secondary structure features and well-resolved high-resolution details, indicating minimal disruption from CTF zero-crossing effects.

We further analyzed CTF compensation in single-micrograph reconstructions and examined the contributions of electron dose to high-resolution structure determination. Our results demonstrate that cryo-EM SPA is capable of resolving near-atomic-resolution structures using a single micrograph and a limited number of particles. These findings offer new insights into optimizing cryo-EM workflows. Reducing the cumulative radiation dose or the number of particles required for high-resolution reconstruction could enhance data acquisition efficiency and minimize radiation damage, especially in future cryo-electron tomography (cryo-ET) applications.

Results

Near-Atomic Resolution 3D Reconstruction from a Single Cryo-EM Micrograph

We first investigated the minimum number of particles required to achieve near-atomic resolution (~3 Å) for single-particle 3D reconstruction of apoferritin. Apoferritin specimens were prepared using graphene-coated grids, and micrographs were collected at regions with optimal ice thickness. As a benchmark for data quality, we reconstructed a high-resolution 3D map from 41,944 particles extracted from 148 micrographs, yielding a 2.2 Å resolution structure approaching the acquisition Nyquist frequency. Well-defined side-chain densities confirmed the high quality of the dataset (Supplementary Fig. 1).

To quantify the relationship between reconstruction resolution and the number of particles, we applied the Rosenthal-Henderson B-factor plot method[13]. Subsets of particles with exponentially increasing counts were randomly sampled from the full dataset and reconstructed *de novo* under consistent refinement parameters. By linearly fitting the achieved resolutions against the natural logarithm of the particle number, ln(N), we estimated the B-factor of the dataset via least-squares fitting. The interpolation of this fit predicted the minimum number of ideal particles required to reach 3.0 Å for apoferritin (Fig. 1a). Under our recorded particle quality, the fit indicated that

~400 particles would suffice. Given that each cryo-EM micrograph acquired at a nominal magnification of 105,000× typically contained 300 to 400 apoferritin particles, we selected a representative micrograph with uniform particle distribution (micrograph No.006) for single-micrograph reconstruction test (Fig. 1b). The power spectrum of the post-correction micrograph showed well-defined Thon rings extending beyond the first water ring (Fig. 1c), consistent with well-preserved high-resolution features.

From this single micrograph, 325 particles were extracted and processed through a standard *de novo* reconstruction workflow, yielding a 3D map at 3.1 Å resolution (Fig. 1f). To further improve reconstruction quality, we performed per-particle CTF refinement and Bayesian polishing to minimize B-factor contributions from beam-induced motion and optical aberrations (Fig. 1f). Through iterative optimization, typically two refinement cycles, we obtained high-resolution density maps at 2.9 Å with sharpened side-chain features and convergence of structural detail and resolution to optimal values (Fig. 1d, Supplementary Fig. 2a). Side-chain density agreed closely with the fitted atomic model, reflecting high map quality (Fig. 1e).

To assess reproducibility, we applied the same single-micrograph analysis workflow to two additional randomly selected micrographs from the same dataset (#001 and #031), yielding reconstructions at 3.1 Å and 3.2 Å, respectively (Supplementary Fig. 3a, b). Using an external apoferritin dataset from the EMPIAR database (EMPIAR-10424[15]), we also successfully reconstructed a 3.0 Å map from a single micrograph containing 134 particles (Fig. 1g and Supplementary Fig. 2b). We further validated the generalizability of our workflow on a different sample, obtaining a 3.4 Å reconstruction of 20S proteasome from a single micrograph containing 434 particles (Fig. 1h and Supplementary Fig. 2c).

Together, given high-quality samples and imaging conditions, single-micrograph datasets containing just a few hundred particles can be sufficient for near-atomic resolution single-particle reconstruction.

Defocus Compensation in Single-Micrograph Cryo-EM Single-Particle 3D Reconstruction

As the image formation in TEM is modulated by the CTF, for a single micrograph recorded at a fixed defocus loses signal at specific spatial frequencies due to the zero crossings. Accordingly, data are typically acquired as a defocus series spanning over 500 nm to recover the affected

spatial frequencies completely. However, our results above demonstrated that high-resolution 3D reconstructions can be achieved using particles from a single micrograph, without evident loss of information at specific spatial frequencies. This observation prompted us to investigate how information near CTF zero crossings is effectively compensated in single-image reconstructions.

The presence of residual objective lens astigmatism introduces directional anisotropy, which consequently distorts the Thon rings from circular to elliptical. This effect results in a pair of orthogonal defocus for each micrograph in the estimated CTF across reciprocal space. For the apoferritin micrograph #006, the estimated defocus along two orthogonal directions were -0.94 µm and -1.01 µm. We first examined the impact of these defocus values on the CTF. The corresponding CTFs for the minimum (−0.94 µm), maximum (−1.01 µm), and midpoint (−0.975 µm) defocus values exhibit similar behavior at low spatial frequencies but diverge at higher frequencies, complementing other's CTF zeroes (Fig. 2a). Notably, the resolution limit of the 3D reconstruction from this single micrograph coincides with the spatial frequency at which all three CTF curves next intersect (Figure 2b), indicating signal loss around that frequency.

We next examined the per-particle defocus distribution in 3D reconstruction from micrograph #006. The particles exhibit an approximately linear defocus gradient of ~300 Å along the Z-axis, indicating different particle Z heights within the vitrified sample. Considering an astigmatism value of 350 Å, each particle effectively experiences a unique defocus in different directions in reciprocal space. The spread in minimum and maximum defocus values across particles therefore reflects both their Z-height distribution and the objective lens astigmatism. Since the particle-specific envelope function A(k) is difficult to quantify, we focused our CTF analysis solely on the oscillatory behavior and neglect the amplitude attenuation component. We modeled the effects of both particle Z-height variation and astigmatism on the compensation of information loss at CTF zeroes.

Each of the reconstructed 325 particles occupies a unique Z-position with a pair of estimated orthogonal defocus values (U and V). We first treated the resulting 650 defocus values as discrete data points and examined their collective modulation effect in reciprocal space. We found that the Z-distribution of particles partially compensates information loss at CTF zero-crossings. The resulting 1D averaged |CTF| curve (Figure 2c, green) shows partial compensation of signal loss at CTF zero crossings. At high spatial frequencies, the lower envelope of the curve lifts off from

the x-axis, indicating reduced occurrence of zero crossings, although the compensation remains modest.

To more realistically simulate the smooth variation in defocus directions across Fourier space introduced by astigmatism, we uniformly sampled 10,000 defocus values within a ~300 Å range, from -0.94 to -1.01 μm, and computed the average of their corresponding 1D |CTF| curves (Figure 2c, yellow). The average of CTFs from these re-sampled defocus values results in significant compensation of missing information, especially at high spatial frequencies. This effect is more prominent in the high-frequency range, likely due to the faster oscillations of the CTF at these frequencies.

In experimental conditions, the CTF modulation across the dataset can be considered as the ensemble effect of numerous particle-based elliptical 2D CTFs. In conventional CTF estimation, astigmatism is accounted for to improve initial fitting accuracy. Software like GCTF and CTFFIND4 employ Equi-phase Averaging (EPA), which enhances 1D signal curves by averaging amplitudes along elliptical contours of equal CTF phase. They then perform 1D cross-correlation searches followed by 2D fitting to refine astigmatism parameters. In contrast, to assess how Z-height variation and astigmatism jointly mitigate zero-crossing losses, we adopted rotational averaging over equal spatial frequency rings in reciprocal space. This approach captures the direction-dependent variation of defocus from real data and its effect on signal recovery at a given spatial frequency. Specifically, we summed the 2D |CTF| amplitudes for all particles and performed rotational averaging over each Fourier ring (orange curve in Figure 2d), producing what we term the “simulated CTF”. When plotted with the FSC curve (Figure 2d), the simulated CTF shows oscillations synchronized with the FSC across both low and high spatial frequencies, indicating that simulated CTF captures the effective modulation behavior of the dataset. A similar analysis on a single-micrograph reconstruction of the 20S proteasome yielded consistent results.

Why do the simulated CTF and FSC curves remain synchronized in frequency even after CTF correction in 3D reconstruction? A likely explanation is the Wiener filter used during CTF correction, which imposes frequency-dependent weighting on the signal and leaves residual signatures in the data, particularly in regions of low SNR. The Wiener filter is defined as:

$$F(k) = \frac{H^*(k)}{|H(k)|^2 + \frac{1}{SNR}} \quad (3)$$

where *H(k)* is the CTF.

For spatial frequencies with high SNR, the filter amplifies the signal. In contrast, for low-SNR frequencies, the filter suppresses the signal, which increases the noise level. This leads to reduced correlation between independently reconstructed half-maps in these frequency bands, thereby lowering the FSC. As a result, the FSC and simulated CTF curves exhibit synchronized oscillations across most spatial frequencies, reflecting this intrinsic filtering effect.

Analysis of the Minimum Cumulative Electron Dose Required for High-Resolution 3D Reconstruction

The high consistency of imaging conditions within a single cryo-EM micrograph allows a controlled test of the minimum cumulative electron dose and SNR required to reach ~3 Å resolution. In SPA, particle images from different projection directions are aligned and averaged, reinforcing shared structural features while random noise is attenuated as the number of particles increases. The correct assignment of reconstruction parameters, especially the Euler angles and in-plane shifts, is critical for high-quality reconstruction. Thus, the minimum required dose and SNR must be sufficient to provide reliable low-to-medium spatial frequency signals for orientation determination and adequate high-frequency signal for achieving near-atomic resolution.

There are two principal strategies to lower the cumulative reconstruction SNR: (1) reducing the total electron dose deposited on the specimen, or (2) decreasing the number of particles used in 3D reconstruction. Since each cryo-EM micrograph is collected as a movie stack, we can generate datasets with different effective doses by summing only the initial set of frames from the stack and evaluating the resulting reconstructions. To achieve this, we performed a series of computational experiments by progressively summing the first n frames (n = 1, 2, ..., 32) from each movie stack. Each frame corresponds to an exposure dose of 1.5625 $e^-/Å^2$, summing to a total dose of 50 $e^-/Å^2$ over 32 frames. Using 325 particles from the apoferritin micrograph #006, we performed *ab-initio* 3D reconstructions without prior information. As shown in Figure 3 (left panels of each group), a global angular search yielded a 2.94 Å resolution

map with an 8-frame dose (12.5 e^{-}/Å^2). When using local refinement, a comparable 2.98 Å map could be obtained with only 7 frames (11.0 e^{-}/Å^2). This is consistent with the notion that fine angular searches require less low-frequency signal. As cumulative dose increased, side-chain densities emerged in the maps. However, little to no additional benefit was observed for the high-resolution features contributed by the final 8 frames (dose range: 37–50 e^{-}/Å^2). We then extended our analysis to 17,575 particles randomly selected from 62 apoferritin micrographs. Remarkably, a dose of only 9.3 e^{-}/Å^2 (6 frames) was sufficient to achieve 2.42 Å resolution through global orientation search (Figure 4, left panels).

To assess the information content of individual frames, we extracted single-frame particle images and reconstructed 3D maps using previously determined alignment parameters (Euler angles and in-plane translations), bypassing the alignment step. For both the 325-particle and 17,575-particle datasets, reconstruction quality decreased monotonically along exposure. In individual-frame dataset reconstructions, cumulative doses above 30 e^{-}/Å^2 showed almost complete loss of high-frequency information (Figure 3, right panels). In the larger dataset, frames 1–8 (below 12.5 e^{-}/Å^2) still yielded well-defined backbone densities and discernible side chain features (Figure 4, right panels), enabled by higher SNR from averaging more particles. Reconstructions from frames 9–19 (14.0–30.0 e^{-}/Å^2) show progressively increasingly blurred side-chain densities, and beyond frame 20 (31.2–50.0 e^{-}/Å^2) even α-helical features faded, indicating substantial radiation damage at higher doses.

Assuming each particle of equal quality contributes identically to orientation determination, the overall SNR of 3D reconstruction becomes a function of both total exposure dose and number of particles (Figure 5a,b). While signal increases with averaging, Gaussian-distributed random noise remains statistically unchanged. Consistent with prior reports and the results above, high spatial frequency signals are more vulnerable to radiation damage than low-frequency components, leading to a faster decay of signal amplitude and the accumulation of high-frequency noise. This noise is manifested as an elevated B-factor (B_image) in Gaussian attenuation models and amplified during map sharpening, thereby diminishing the contrast of high-resolution features (Supplementary Figure 3c, d). Optimal resolution in our data was achieved when the cumulative dose of 12–14 e^{-}/Å^2 (Appendix Figure 3a,b). For small particles, the reduced high-frequency

SNR can significantly compromise the accuracy of orientation determination, contributing to a larger computational B-factor (B_computation) due to angular misassignments.

Following previous studies, we related SNR(k) to FSC(k) and modeled ln(SNR) versus cumulative dose per resolution shell by linear regression[16]:

$$\mathrm{SNR}(k) = \frac{2\mathrm{FSC}(k)}{1 - \mathrm{FSC}(k)} \tag{4}$$

We adopted this approach to compare the SNR from 325 particles at 12.5 $e^-/Å^2$ with that from particles exposed to a full 50 $e^-/Å^2$ dose. Given that apoferritin is significantly smaller than the double-layered rotavirus particles used in Grigorieff's study, we grouped the 62 micrographs by every 3 frames (4.6 $e^-/Å^2$) to estimate the critical exposure curves. Figure 5a shows linear fits of ln(SNR) vs. dose for six representative resolutions. SNR increases linearly with particle number across spatial frequencies (Figure 5b). For a total dose of N $e^-/Å^2$, the SNR can be modeled as:

$$\mathrm{SNR}(k, N) = \mathrm{SNR}(k, 0)\mathrm{e}^{-\frac{N}{\mathrm{N_e}(k)}} \tag{5}$$

Based on the fitted parameters, the total SNR required to achieve accurate 3 Å resolution reconstructions from 325 particles at 12.5 $e^-/Å^2$ (K_b) can be estimated as equivalent to n particles at 50.0 $e^-/Å^2$ (K_a):

$$325 \times \sum_i \sum_{k=1}^{Kb} e^{-a_i k + b_i} = n \times \sum_i \sum_{k=1}^{Ka} e^{-a_i k + b_i} \tag{6}$$

where $ln(SNR) = -a_i d_k + b_i$ is the linear fit for each resolution shell i, and k represents cumulative dose. Solving this equation for K_a = 50.0 $e^-/Å^2$ and K_b = 12.5 $e^-/Å^2$ yields n = 180.

Therefore, 325 particles at 12.5 $e^-/Å^2$ were sufficient for a 3 Å resolution reconstruction from a global angular search, and equivalently, 180 particles at 50.0 $e^-/Å^2$ should suffice for the same task without any prior orientation knowledge (Figure 5c). Due to the relatively small sample size and specific structural features, linear regression at certain resolutions was less accurate. Hence, frequencies with poor fit were omitted from subsequent estimation. Consequently, the calculated particle number should be treated as a qualitative benchmark rather than an absolute value.

We then validated these predictions empirically. Random subsets from micrograph #006 showed that 182 particles at 50 $e^{-}/Å^{2}$ achieved ~3 Å resolution, consistent with the prediction and with reconstructions from 325 particles at 12.5 $e^{-}/Å^{2}$ (Figure 5d). Finally, since the final 8 frames contribute little due to severe radiation damage to high-frequency information, we further performed an additional reconstruction using 189 particles and only the first 24 frames (cumulative dose of 36.0 $e^{-}/Å^{2}$), excluding the last 8 frames. This resulted in a 2.9 Å resolution map reconstructed *de novo*. Under the optimal dose conditions of 36.0 $e^{-}/Å^{2}$, 189 particles represent the minimum required particle number from this apoferritin dataset to reach ~3 Å resolution.

Discussion

In this study, we demonstrate that near-atomic resolution three-dimensional (3D) reconstructions of apoferritin and the 20S proteasome can be achieved using cryo-EM SPA with as few as several hundred particles from a single micrograph. For apoferritin, a 3.0 Å map was obtained from just 134 particles from a single micrograph downloaded from EMPIAR. Given the 24-fold octahedral symmetry of apoferritin, this result suggests that approximately 3,200 asymmetric units of comparable image quality and accurately assigned orientations may be sufficient to yield near-atomic resolution reconstructions.

The successful single-micrograph reconstruction underscores the potential of high-quality cryo-EM data to significantly reduce the need for excessive data redundancy[17]. During large-scale data screening, deep 2D classification is commonly used to eliminate low-quality data due to damaged structures or preferred orientations. However, if particles only exhibit localized structural variations without large-scale changes in overall conformation or domain composition, standard 3D classification methods may struggle to separate heterogeneous particles based on correlation metrics. Such particles can be misoriented or blur high-resolution features, effectively inflating computational B-factors and further amplifying artifacts during sharpening. Improving the structural homogeneity of macromolecular particles in cryo-EM specimens therefore substantially reduce dataset size and computationally induced B-factors. In general, enhancing cryo-EM sample quality enables smaller datasets to yield high-resolution reconstructions more efficiently.

To date, the prevailing need for very large SPA datasets largely reflects suboptimal specimen quality. Contributing factors include: First, inappropriate ice thickness can lead to excessive background noise. Second, during blotting and thinning of the liquid film, macromolecules tend to adsorb to the air-water interface, resulting in preferred orientation, denaturation, or dissociation of complexes. Third, structural heterogeneity, either in composition or conformation, can hinder high-resolution reconstruction. If these problems can be effectively addressed, high-resolution SPA may be possible from only a few micrographs, or even a single one. Recent advances in cryo-EM grid supports, sample preparation equipment, and biochemical stabilization methods have made progress in overcoming these limitations[18-22]. The graphene support films used in this study also played a significant role in preserving sample integrity.

We also systematically examined the impact of cumulative electron exposure on structural information retention in cryo-EM data collection. Early frames acquired at low cumulative doses experience minimal radiation damage and retain intact high- and low-frequency signals. Using pre-determined angular parameters, particles from the first three frames contain sufficient information to resolve side chain features. While early frames are sometimes discarded due to their susceptibility to beam-induced motion, our analysis confirms that these frames contain minimally damaged high-frequency signals that are essential for achieving high-resolution reconstructions. By leveraging known Euler angles and bypassing alignment, we verified the fidelity of both high- and low-frequency information and assessed the accuracy of beam-induced motion correction in early frames. Conversely, frames exposed to higher cumulative doses (e.g., >30 $e^{-}/Å^{2}$) suffer from pronounced radiation damage. High-frequency signal decays rapidly relative to low-frequency components. Truncating late frames or lowering total dose suppresses high-frequency noise in the final reconstruction even with dose-weighting.

For any target resolution, the minimum signal required for accurate reconstruction is jointly determined by the number of particles and their optimal cumulative exposure. By quantifying dose-dependent decay of low- and high-resolution signal and relating dose to SNR, we confirmed that a 2.9 Å reconstruction is attainable with 325 particles at only 12.5 $e^{-}/Å^{2}$. Under equivalent total SNR, ~180 particles suffice to reach ~3 Å at 50.0 $e^{-}/Å^{2}$.

Our findings indicate that, compared to conventional protocols, near-atomic resolution reconstructions can be achieved with either lower electron doses or fewer particles. The

principles may also benefit cryo-electron tomography (cryo-ET). In cryo-ET, tilt series are collected at multiple angles with dose accumulation over the series. Despite operating in low-dose mode, radiation damage can significantly compromise high-frequency signals particularly at high tilt angles under dose-symmetric schemes. In future work, we aim to refine cryo-ET data acquisition strategies to determine the minimum SNR and dose requirements necessary for high-resolution subtomogram averaging. This approach has the potential to capture critical high-frequency information with less redundant data, thereby improving overall efficiency in cryo-ET.

Figures and Figure Legends

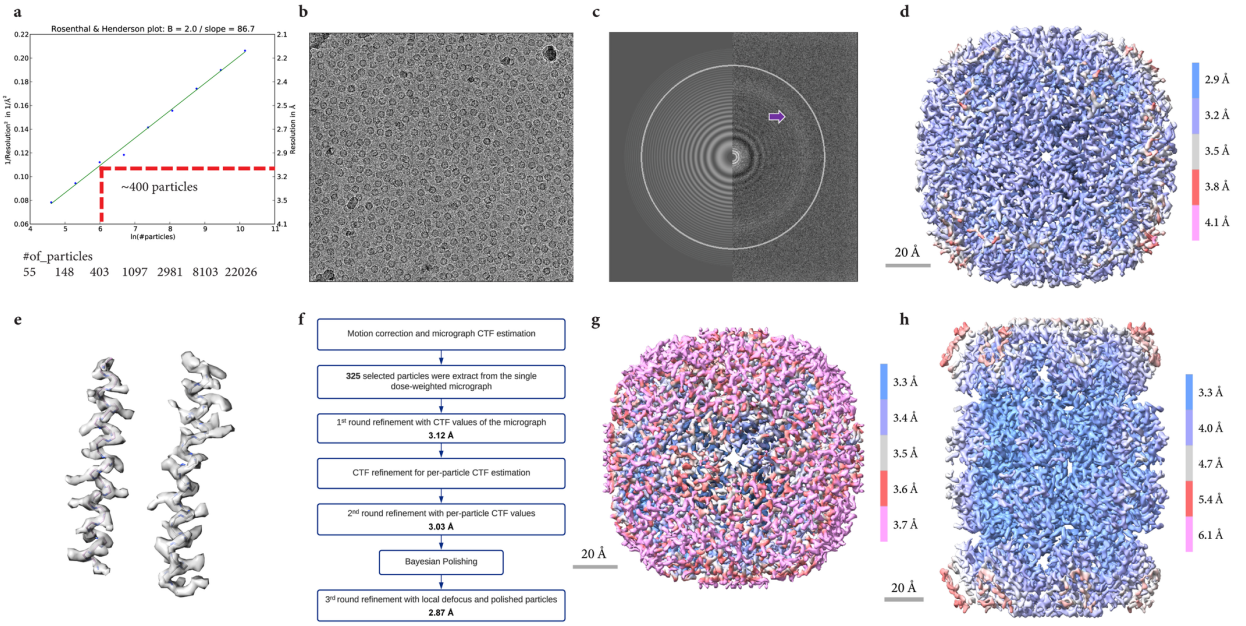

Fig. 1 Near-atomic resolution 3D reconstruction of apo-ferritin from a single micrograph. a. A schematic Rosenthal-Henderson plot showing the natural logarithm of particle count, ln(*N*), as a function of the reciprocal of resolution squared ($1/d^2$); b. A total of 325 particles were selected from an aligned and merged movie sum of apo-ferritin, imaged with a total exposure of 50 $e^-/Å^2$ (micrograph #006); c. Power spectrum of the selected micrograph. The Thon rings are evident beyond the water ring at 3.7 Å resolution (Purple arrow). White circles indicate the outermost visible Thon ring; d. 3D reconstruction of the 325 apo-ferritin particles from a single micrograph, achieving a resolution of 2.9 Å; e. Zoomed-in view of the 3D map in panel (d), highlighting local side-chain densities of α-helices; f. Data processing workflow of the single-micrograph reconstruction; g. 3D reconstruction of mouse heavy-chain apoferritin (Raw data: EMPIAR-10424) from 134 particles on a single micrograph at a resolution of 3.0 Å; h. 3D reconstruction of the 20S proteasome from 434 particles on a single micrograph, achieving 3.5 Å resolution.

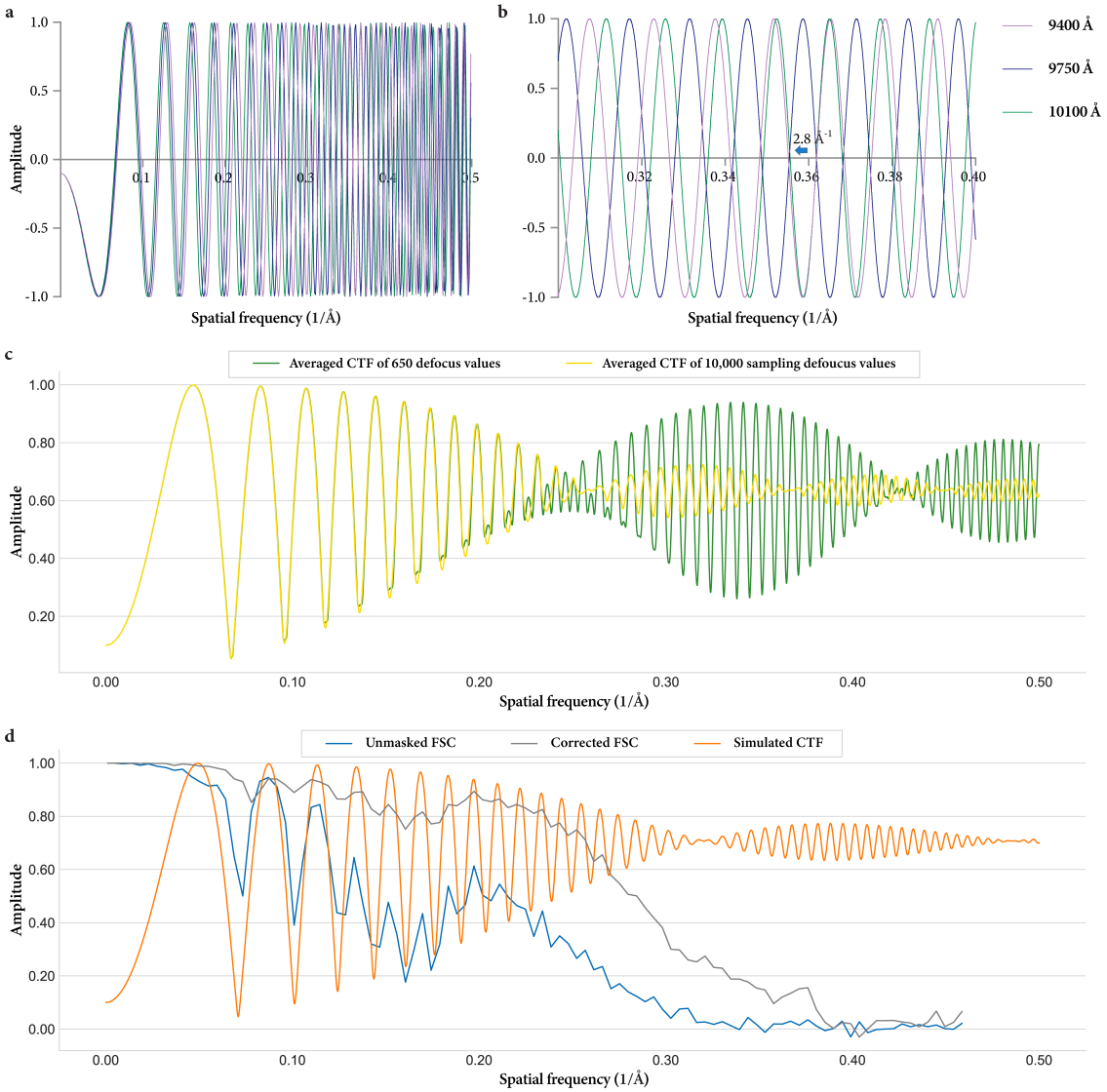

Fig. 2 Compensation for missing information at CTF zero-crossings. a. CTF curves for two endpoints (0.94 and 1.01 μm) of the defocus interval and the median value (0.975 μm); b. Zoomed-in view of the high-frequency region in panel a, showing phase complementation at zero-crossings due to alternating non-zero values from CTF oscillations; c. The average of |CTF| of 650 defocus values sampled from per-particle defocus U and defocus V of 325 reconstructed particles (green curve). The average of |CTF| of 10,000 uniformly sampled defocus values within the same defocus range (yellow curve), indicating compensation of CTF zeroes through particle defocus distribution and astigmatism; d. Simulated CTF plot for the 325 particles, showing the effect of Z-axis distribution and astigmatism on compensating for missing structural information at CTF zeroes. FSC curves with and without masking (blue and gray, respectively) show synchronized oscillations with simulated CTF in both low- and high-frequency regions.

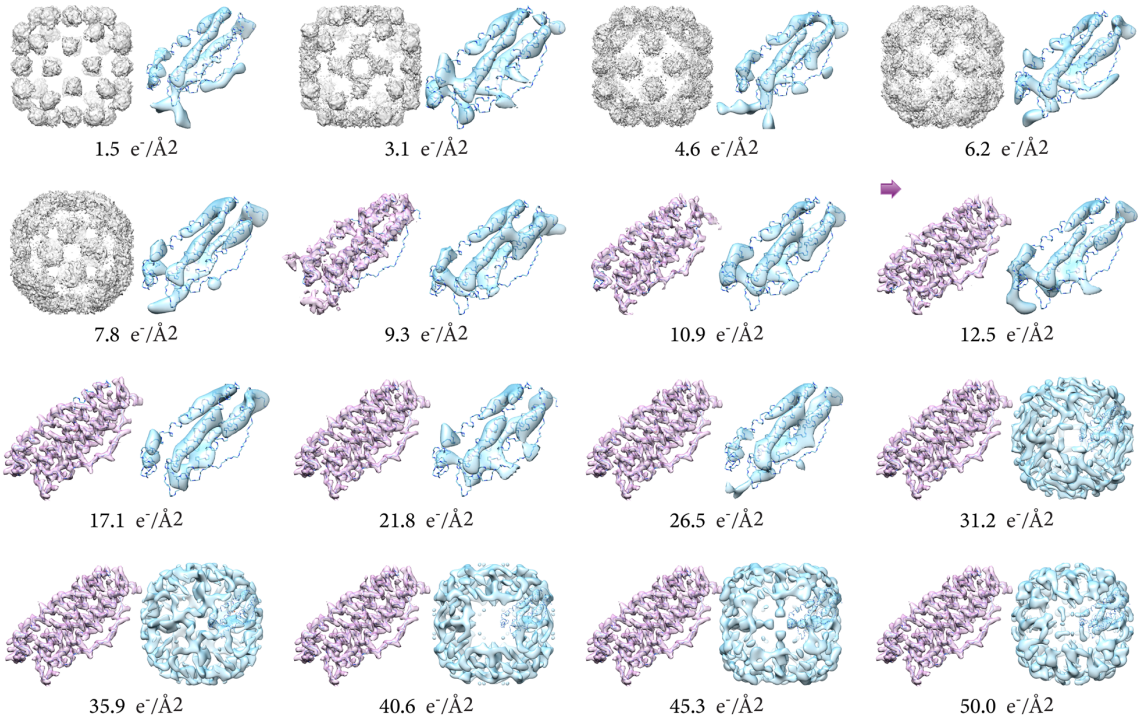

Fig. 3 3D reconstruction at varying cumulative electron doses. Reconstruction results from 325 particles at varying exposure doses (1.56–50 $e^{-}/Å^2$) are shown for both full-frame (left, purple) and individual-frame (right, blue) processing. The 3D reconstruction from 325 particles at a dose of 12.5 $e^{-}/Å^2$ (8 frames) refined to 2.9 Å resolution (purple arrow).

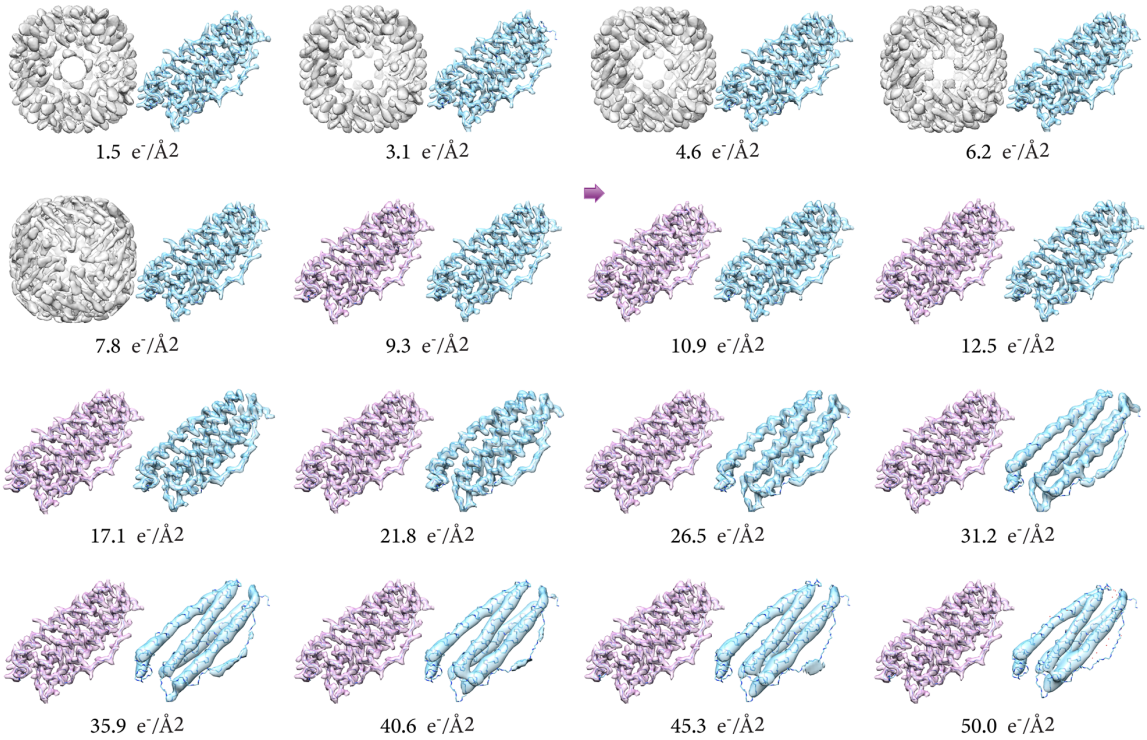

Fig. 4 Enlarged dataset reconstruction at varying electron doses. Reconstruction results from 17,575 particles processed with different cumulative exposure doses (1.56–50 $e^{-}/Å^{2}$) are shown for full-frame (left, purple) and single-frame (right, blue) data. The reconstruction at 10.9 $e^{-}/Å^{2}$ (7 frames) refined to 2.3 Å resolution (purple arrow).

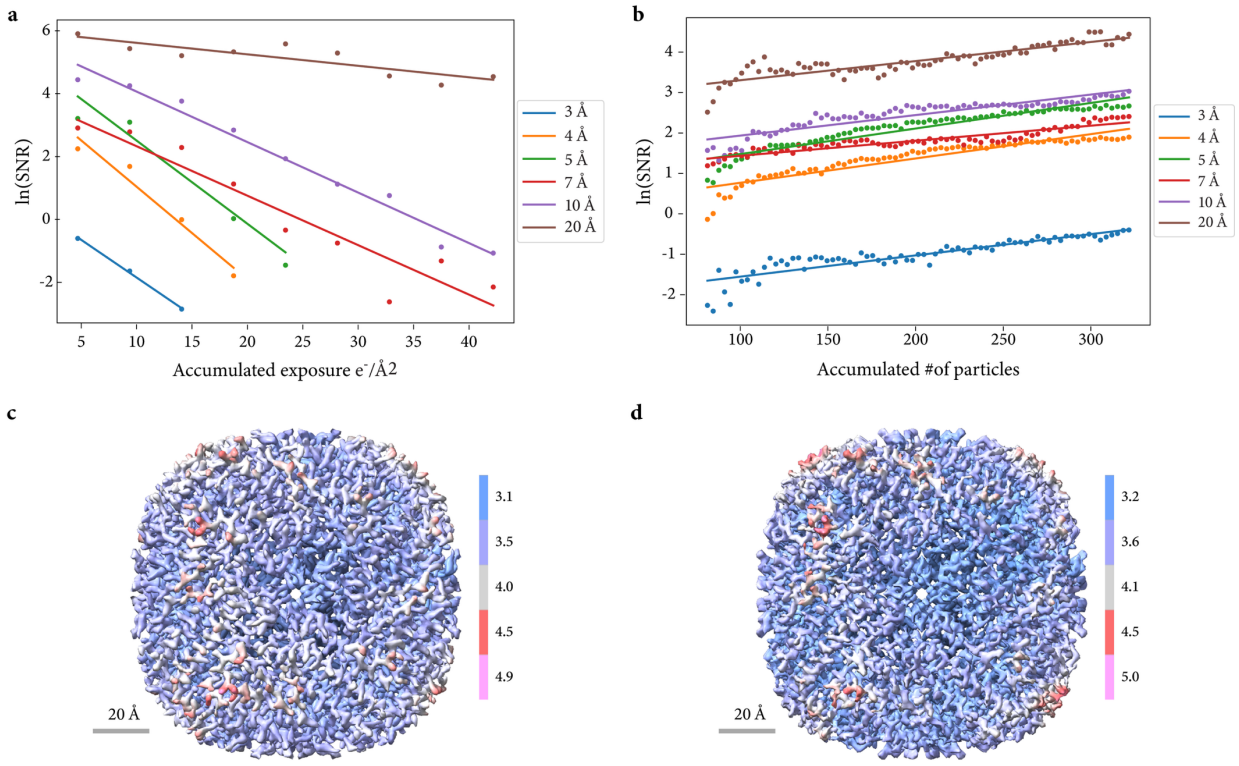

Fig. 5 SNR in high-resolution reconstruction. a. Linear fits for ln(SNR) versus cumulative dose at different resolutions, showing that ln(SNR) declines more rapidly at higher resolution; b. Linear fits of ln(SNR) versus particle count at a total dose of 50 e^{-}/Å² for different resolutions, indicating ln(SNR) increases with the number of particles. For high-frequency signals, 180 particles at 50 e^{-}/Å² yield ln(SNR) value comparable to those from 325 particles at 12.5 e^{-}/Å²; c. Global refinement of the 325 particles at 12.5 e^{-}/Å² yielded a ~3.0 Å reconstruction, comparable to that obtained from a random subset of 189 particles at 50 e^{-}/Å² in panel d.

Methods

Sample Preparation for Single-Particle Cryo-EM

Human heavy-chain apoferritin[23] and *Thermoplasma acidophilum* 20S proteasomes[9] were prepared following previously described protocols. Quantifoil R0.6/1 300-mesh gold grids were glow-discharged using a Harrick Plasma cleaner. After a 2-minute evacuation, grids were treated at “medium” power for 30 seconds (standard Quantifoil) or “low” power for 15 seconds (graphene-supported grids) to render the surface hydrophilic.

For vitrification, 4 μL of 1 mg/mL apoferritin or 20S proteasome protein solution was applied to freshly glow-discharged grids inside a Vitrobot Mark IV (Thermo Fisher Scientific). The blot force was set to -2, with a blot time of 4 seconds. Grids were then rapidly plunged into liquid ethane cooled to liquid nitrogen temperature and subsequently transferred to liquid nitrogen storage for long-term preservation.

SPA Data Acquisition

Cryo-EM imaging was performed on a 300-kV FEI Titan Krios transmission electron microscope (TEM D3424) equipped with a spherical aberration (Cs) corrector, a K2 Summit direct electron detector with Gatan BioQuantum energy filter. Both apoferritin and 20S proteasome samples were loaded into the microscope and imaged in energy-filtered transmission electron microscopy (EFTEM) mode using nanoprobe illumination under low-dose conditions.

A 50 μm C2 aperture was used with a nominal magnification of 105,000×, resulting in a calibrated pixel size of 0.5455 Å at the specimen level. Micrographs were collected with a defocus range of -0.8 to -1.5 μm. The microscope was carefully aligned, , and the Cs corrector was finely tuned before data collection. Camera background subtraction and gain reference correction were performed prior to data acquisition. A total electron dose of 50 $e^{-}/Å^{2}$ was used , and the energy-filter slit width was properly adjusted and centered. Automated data acquisition was carried out using AutoEMation software[24], with 2.56 seconds exposure time and fractionated as 32 super-resolution movie frames.

SPA Data Processing

Pre-processing: Raw movies were converted from .dat to .mrcs format using dat2mrc, a custom program developed at the Tsinghua University Cryo-EM Facility. Real-time drift correction was conducted using TsinghuaSoftwares.py, which integrates MotionCor2-1.6.3[25]. Dose weighting was applied to individual frames based on accumulated exposure and spatial frequency. Defocus and astigmatism values were estimated using CTFFIND4[26] and GCTF[27], and high-quality micrographs were selected for downstream analysis.

Particle Picking and Classification: Particle picking was performed via both template-based methods in RELION-3.1[28] and deep learning-based approaches using Topaz. Extracted particles were boxed with a box size approximately 1.3× of the particle diameter. Two-dimensional (2D) classification was performed to identify representative particle views, ensuring diverse angular sampling rather than strict outlier exclusion.

3D Reconstruction and Refinement: Three-dimensional (3D) classification and refinement were performed using a combination of global and local searches in RELION-3.1[28], RELION-4.0[29], and cryoSPARC v4.2[30].

Post-processing: Final reconstructions were postprocessed using the RELION postprocessing module. The resolution of each reconstruction was estimated at the 0.143 Fourier shell correlation (FSC) criterion. B-factor sharpening was applied to enhance high-resolution structural features.

Model Building and Validation: Atomic model building and structure analysis were carried out in UCSF Chimera v1.17[31] and ChimeraX v1.6[32]. Homologous crystal structures were docked into the cryo-EM maps using the “Fit in Map” tool in ChimeraX. Manual adjustments of amino acid side chains were performed residue by residue in COOT[33]. Final real-space refinement was conducted in PHENIX v1.19[34], with special attention to the geometry and stereochemistry of side chains and backbone traces.

Data Analysis

One-dimensional radially averaged power spectra were computed using custom Python scripts based on CTF parameters after CTF estimation.

Acknowledgements

We thank Dr. Jianlin Lei, Dr. Xiaomin Li, Dr. Fan Yang, and Dr. Tao Yang at the Technology center for protein sciences at Tsinghua University (Beijing) for their valuable technical support with cryo-EM data collection and high-performance computing.

Ethics declarations

The authors declare no competing interests.

Supplementary Information

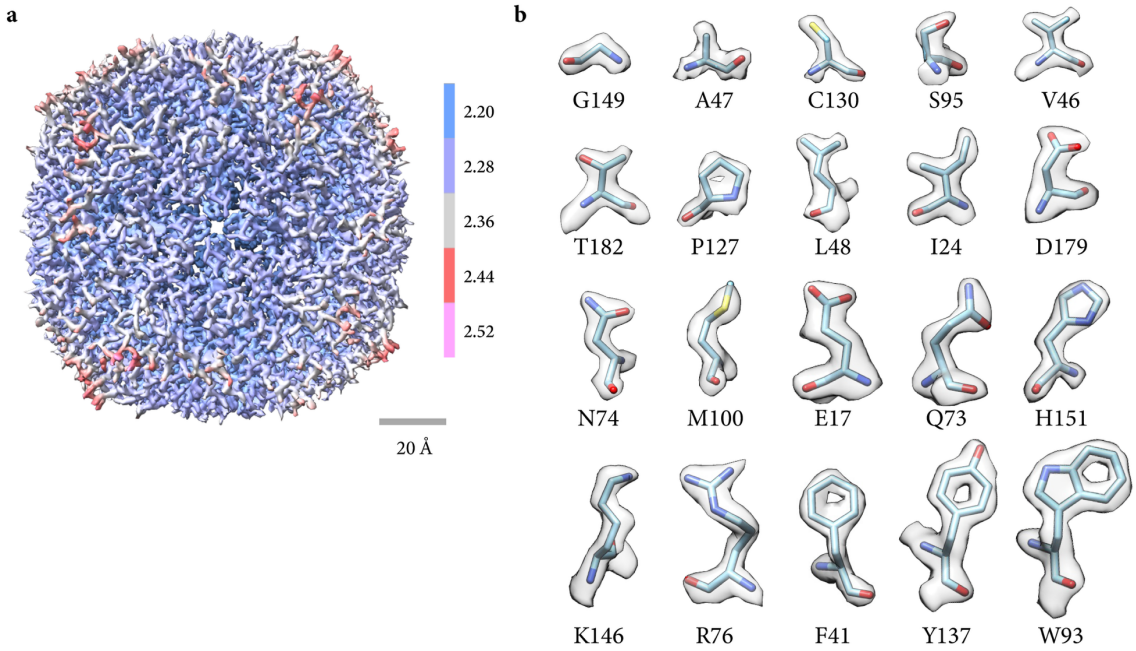

Supplementary Fig. 1 Single-particle 3D reconstruction of the complete apoferritin dataset. a. The 3D density map of the complete apoferritin dataset reaches a resolution of 2.2 Å; b. The local apoferritin density map shows well-resolved side chains align closely with the atomic model, confirming the quality of high-resolution the reconstruction.

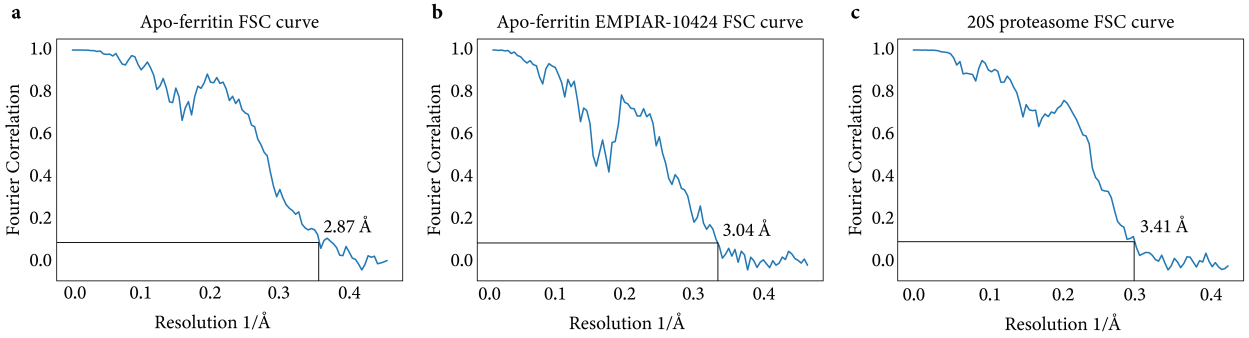

Supplementary Fig. 2 FSC curves of 3D reconstructions from single micrographs. a. FSC curve of the single-micrograph particle reconstruction from the apoferritin dataset collected in this study; b. FSC curve of the single-micrograph particle reconstruction from the EMPIAR-10424 apoferritin dataset; c. FSC curve of the single-micrograph particle reconstruction from the 20S proteasome dataset collected in this study.

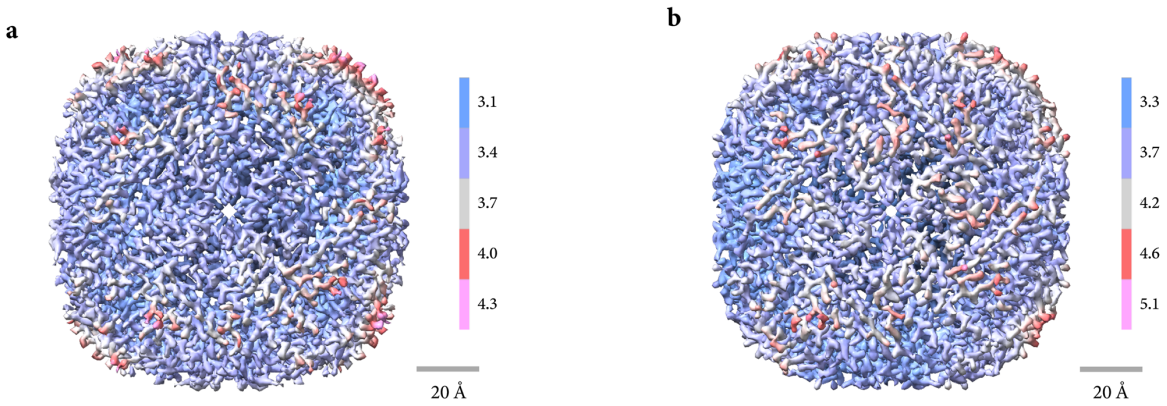

Supplementary Fig. 3 Reproducibility of single-micrograph 3D reconstructions of apoferritin. The reconstructions from a single micrograph (a) (#001, 313 particles) and another micrograph (b) (#031, 229 particles) reached resolutions 3.1 Å and 3.2 Å, respectively.

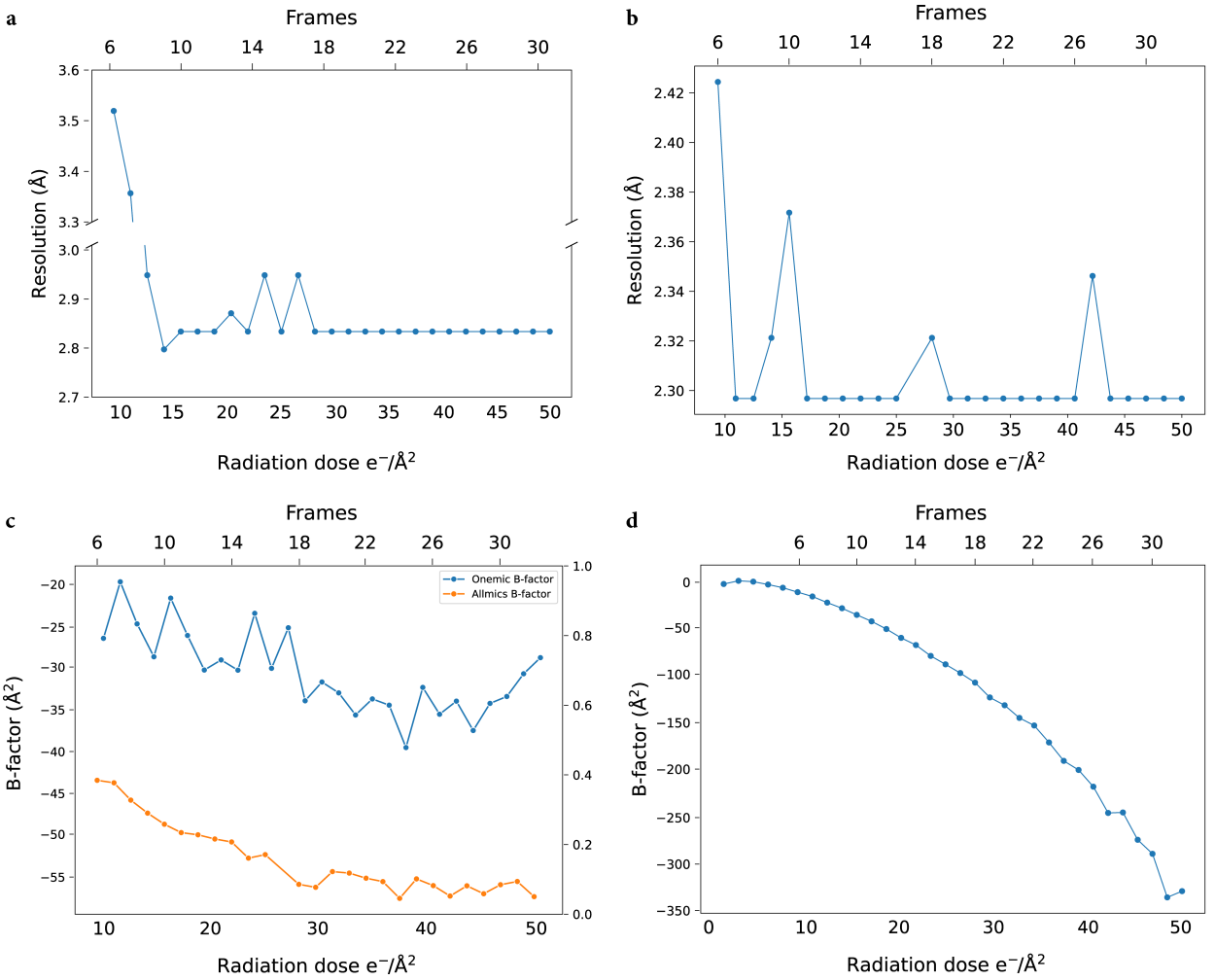

Supplementary Fig. 4 Relationship between radiation dose, resolution, and B-factor. a. Resolution of reconstructions from a single micrograph (325 particles); b. and from a larger dataset (62 micrographs, 17,575 particles) as a function of cumulative exposure. c. Relationship between B-factor and radiation dose for single micrographs (blue line) and larger datasets (orange line); d. Frame-wise B-factor applied during Bayesian polishing.

References:

1 Cheng, Y., Grigorieff, N., Penczek, P. A. & Walz, T. A Primer to Single-Particle Cryo-Electron Microscopy. *Cell* **161**, 438-449 (2015). https://doi.org/10.1016/j.cell.2015.03.050

2 Frank, J. Single-particle imaging of macromolecules by cryo-electron microscopy. *Annu Rev Biophys Biomol Struct* **31**, 303-319 (2002). https://doi.org/10.1146/annurev.biophys.31.082901.134202

3 Kuhlbrandt, W. Biochemistry. The resolution revolution. *Science* **343**, 1443-1444 (2014). https://doi.org/10.1126/science.1251652

4 Nogales, E. The development of cryo-EM into a mainstream structural biology technique. *Nat Methods* **13**, 24-27 (2016). https://doi.org/10.1038/nmeth.3694

5 Peplow, M. Cryo-Electron Microscopy Reaches Resolution Milestone. *ACS Central Science* **6**, 1274-1277 (2020). https://doi.org/10.1021/acscentsci.0c01048

6 Saibil, H. R. Cryo-EM in molecular and cellular biology. *Mol Cell* **82**, 274-284 (2022). https://doi.org/10.1016/j.molcel.2021.12.016

7 Van Drie, J. H. & Tong, L. Cryo-EM as a powerful tool for drug discovery. *Bioorganic & Medicinal Chemistry Letters* **30**, 127524 (2020). https://doi.org/https://doi.org/10.1016/j.bmcl.2020.127524

8 Faruqi, A. R. & McMullan, G. Electronic detectors for electron microscopy. *Quarterly Reviews of Biophysics* **44**, 357-390 (2011). https://doi.org/10.1017/S0033583511000035

9 Li, X. M. *et al.* Electron counting and beam-induced motion correction enable near-atomic-resolution single-particle cryo-EM. *Nature Methods* **10**, 584-+ (2013). https://doi.org/10.1038/nmeth.2472

10 Scheres, S. H. A Bayesian view on cryo-EM structure determination. *J Mol Biol* **415**, 406-418 (2012). https://doi.org/10.1016/j.jmb.2011.11.010

11 Chua, E. Y. D. *et al.* Better, Faster, Cheaper: Recent Advances in Cryo-Electron Microscopy. *Annu Rev Biochem* **91**, 1-32 (2022). https://doi.org/10.1146/annurev-biochem-032620-110705

12 Baxter, W. T., Grassucci, R. A., Gao, H. & Frank, J. Determination of signal-to-noise ratios and spectral SNRs in cryo-EM low-dose imaging of molecules. *Journal of Structural Biology* **166**, 126-132 (2009). https://doi.org/https://doi.org/10.1016/j.jsb.2009.02.012

13 Rosenthal, P. B. & Henderson, R. Optimal determination of particle orientation, absolute hand, and contrast loss in single-particle electron cryomicroscopy. *J Mol Biol* **333**, 721-745 (2003). https://doi.org/10.1016/j.jmb.2003.07.013

14 Kayama, Y. *et al.* Below 3 Å structure of apoferritin using a multipurpose TEM with a side entry cryoholder. *Scientific Reports* **11**, 8395 (2021). https://doi.org/10.1038/s41598-021-87183-1

15 Nakane, T. *et al.* Single-particle cryo-EM at atomic resolution. *Nature* **587**, 152-+ (2020). https://doi.org/10.1038/s41586-020-2829-0

16 Grant, T. & Grigorieff, N. Measuring the optimal exposure for single particle cryo-EM using a 2.6 A reconstruction of rotavirus VP6. *Elife* **4**, e06980 (2015). https://doi.org/10.7554/eLife.06980

17 杨梓, 范潇 & 王宏伟. 应用单张冷冻电镜显微照片解析近原子分辨率的单颗粒三维重构. *电子显微学报* **44**, 91-105 (2025).

18 Liu, N. *et al.* Bioactive Functionalized Monolayer Graphene for High-Resolution Cryo-Electron Microscopy. *J Am Chem Soc* **141**, 4016-4025 (2019). https://doi.org/10.1021/jacs.8b13038

19 Liu, N. & Wang, H. W. Better Cryo-EM Specimen Preparation: How to Deal with the Air-Water Interface? *Journal of Molecular Biology* **435** (2023). https://doi.org/10.1016/j.jmb.2022.167926

20 Zheng, L. M. *et al.* Uniform thin ice on ultraflat graphene for high-resolution cryo-EM. *Nature Methods* **20**, 123-+ (2023). https://doi.org/10.1038/s41592-022-01693-y

21 Liu, N. & Wang, H. W. Graphene in cryo-EM specimen optimization. *Curr Opin Struc Biol* **86** (2024). https://doi.org/10.1016/j.sbi.2024.102823

22 Yang, Z. *et al.* Electrospray-assisted cryo-EM sample preparation to mitigate interfacial effects. *Nature Methods* **21**, 1023–1032 (2024). https://doi.org/10.1038/s41592-024-02247-0

23 Fan, X. *et al.* Near-Atomic Resolution Structure Determination in Over-Focus with Volta Phase Plate by Cs-Corrected Cryo-EM. *Structure* **25**, 1623-+ (2017). https://doi.org/10.1016/j.str.2017.08.008

24 Lei, J. L. & Frank, J. Automated acquisition of cryo-electron micrographs for single particle reconstruction on an FEI Tecnai electron microscope. *Journal of Structural Biology* **150**, 69-80 (2005). https://doi.org/10.1016/j.jsb.2005.01.002

25 Zheng, S. Q. *et al.* MotionCor2: anisotropic correction of beam-induced motion for improved cryo-electron microscopy. *Nature Methods* **14**, 331-332 (2017). https://doi.org/10.1038/nmeth.4193

26 Rohou, A. & Grigorieff, N. CTFFIND4: Fast and accurate defocus estimation from electron micrographs. *Journal of Structural Biology* **192**, 216-221 (2015). https://doi.org/10.1016/j.jsb.2015.08.008

27 Zhang, K. Gctf: Real-time CTF determination and correction. *Journal of Structural Biology* **193**, 1-12 (2016). https://doi.org/10.1016/j.jsb.2015.11.003

28 Zivanov, J. *et al.* New tools for automated high-resolution cryo-EM structure determination in RELION-3. *Elife* **7** (2018). https://doi.org/10.7554/eLife.42166

29 Kimanius, D., Dong, L. Y., Sharov, G., Nakane, T. & Scheres, S. H. W. New tools for automated cryo-EM single-particle analysis in RELION-4.0. *Biochem J* **478**, 4169-4185 (2021). https://doi.org/10.1042/Bcj20210708

30 Punjani, A., Rubinstein, J. L., Fleet, D. J. & Brubaker, M. A. cryoSPARC: algorithms for rapid unsupervised cryo-EM structure determination. *Nature Methods* **14**, 290-+ (2017). https://doi.org/10.1038/Nmeth.4169

31 Pettersen, E. F. *et al.* UCSF chimera - A visualization system for exploratory research and analysis. *J Comput Chem* **25**, 1605-1612 (2004). https://doi.org/10.1002/jcc.20084

32 Pettersen, E. F. *et al.* UCSF ChimeraX: Structure visualization for researchers, educators, and developers. *Protein Sci* **30**, 70-82 (2021). https://doi.org/10.1002/pro.3943

33 Emsley, P., Lohkamp, B., Scott, W. G. & Cowtan, K. Features and evelopment of Coot. *Acta Crystallographica Section D-Biological Crystallography* **66**, 486-501 (2010). https://doi.org/10.1107/S0907444910007493

34 Adams, P. D. *et al.* PHENIX: a comprehensive Python-based system for macromolecular structure solution. *Acta Crystallogr D* **66**, 213-221 (2010). https://doi.org/10.1107/S0907444909052925